

# Derivation of depolarization ratios of aerosol fluorescence and water vapor Raman backscatters from lidar measurements

Igor Veselovskii<sup>1</sup>, Qiaoyun Hu<sup>2</sup>, Philippe Goloub<sup>2</sup>, Thierry Podvin<sup>2</sup>, William Boissiere<sup>2</sup>, Mikhail Korenskiy<sup>1</sup>, Nikita Kasianik<sup>1</sup>, Sergey Khaykyn<sup>3</sup>, Robin Miri<sup>2</sup>

<sup>1</sup>*Prokhorov General Physics Institute of the Russian Academy of Sciences, Moscow, Russia.*

<sup>2</sup>*Univ. Lille, CNRS, UMR 8518 - LOA - Laboratoire d'Optique Atmosphérique, F-59650 Lille, France*

<sup>3</sup>*Laboratoire Atmosphère Observations Spatiales, UVSQ, CNRS, Sorbonne University, Guyancourt, France*

**Correspondence:** Qiaoyun Hu (qiaoyun.hu@univ-lille.fr)

## Abstract

Polarization properties of the fluorescence induced by polarized laser radiation are widely considered in laboratory studies. In lidar observations, however, only the total backscattered power of fluorescence is analyzed. In this paper we present results obtained with a modified Mie-Raman-Fluorescence lidar operated at the ATOLL observatory, Laboratoire d'Optique Atmosphérique, University of Lille, France, allowing to measure depolarization ratios of fluorescence at 466 nm ( $\delta_F$ ) and of water vapor Raman backscatter. Measurements were performed in May-June 2023 during the Alberta forest fires season when smoke plumes were almost continuously transported over the Atlantic Ocean towards Europe. During the same period, smoke plumes from the same sources were also detected and analyzed in Moscow, at the General Physics Institute (GPI), with a 5-channel fluorescence lidar able to measure fluorescence backscattering at 438, 472, 513, 560 and 614 nm. Results demonstrate that, inside the planetary boundary layer (PBL), the urban aerosol fluorescence is maximal at 438 nm, then it gradually decreases with increase of wavelength. The smoke layers observed within 4-6 km height present a maximum of fluorescence at 513 nm, while in the upper troposphere, fluorescence maximum shifts to 560 nm. Regarding the fluorescence depolarization ratio, for smoke its value typically varies within the 45-55 % range.

The depolarization ratio of the water vapor Raman backscattering at 408 nm is shown to be quite low ( $2\pm 0.5\%$ ) in the absence of fluorescence, because the narrowband interference filter (0.3 nm) in the water vapor channel selects only the strongest vibrational lines of the Raman spectrum.

32 As a result, the depolarization ratio at the water vapor Raman channel is sensitive to the presence  
33 of strongly depolarized fluorescence backscattering and can be used for evaluation of the aerosol  
34 fluorescence contribution to measured water vapor mixing ratio.

35

## 36 1. Introduction

37 Possibility to measure the laser induced fluorescence becomes an important added-value to  
38 existing Mie-Raman lidars, because fluorescence measurements provide new independent  
39 information about aerosol properties. Nowadays, the spectroscopic lidars based on 32-channel  
40 PMT combined with spectrograph proved the ability to measure the fluorescence spectrum  
41 (Sugimoto et al., 2012; Reichardt, 2014; Reichardt et al., 2018, 2023, Richardson et al., 2019; Liu  
42 et al., 2022). On the other hand, lidars, with a single fluorescence channel can be widespread due  
43 to their simplicity (Rao et al., 2018; Veselovskii et al., 2020). Such single-channel fluorescence  
44 lidar combined with depolarization measurements at the elastic wavelength, provide new  
45 independent information about aerosol type (Veselovskii et al., 2022). However, in all lidar  
46 studies, only the total scattered power was analyzed, while the polarization properties of the  
47 fluorescence were ignored. At the same time, fluorescence depolarization measurements are  
48 widely used in laboratory research (Lakowicz, 2006). When polarized laser radiation is used for  
49 excitation, the fluorescence emission is also partly polarized and degree of its depolarization  
50 (anisotropy) depends on the fluorescence lifetime, on the angle between excitation and emission  
51 dipoles, and on the rotational mobility of molecules (Lakowicz, 2006). In the fluorescence  
52 spectroscopy, the polarization state of emission is described by the anisotropy (Lakowicz, 2006),  
53 introduced as:

$$54 \quad r = \frac{P_F^{\square} - P_F^{\perp}}{P_F^{\square} + 2P_F^{\perp}} \quad (1)$$

55 where  $P_F^{\square}$  and  $P_F^{\perp}$  are the powers of co- and cross-polarized fluorescence components. In lidar  
56 measurements, however, the fluorescence depolarization ratio,  $\delta_F$  is given as.

$$57 \quad \delta_F = \frac{P_F^{\perp}}{P_F^{\square}} \quad (2)$$

58 Therefore, the anisotropy is expressed as a function of the  $\delta_F$  as follows:

$$59 \quad r = \frac{1 - \delta_F}{1 + 2\delta_F} \quad (3)$$

60 For randomly oriented fluorophores with collinear absorption and emission dipoles, in the  
61 absence of rotational motion, the anisotropy  $r=0.4$  (Lakowicz, 2006), which corresponds to  
62  $\delta_F=33\%$ . This is the minimal value one can expect in lidar measurements. Existence of any angle  
63 between absorption and emission dipoles, as well as molecule rotation in the process of emission  
64 will increase  $\delta_F$  (Lakowicz, 2006). Thus, measurement of fluorescence depolarization ratio may  
65 bring additional information about atmospheric aerosol, as we will show below.

66 Water vapor is a key atmospheric component playing essential role in the planet's radiative  
67 balance, and Raman lidars today are widely used for such observations (Whiteman, 2003, Chouza  
68 et al., 2022 and references therein). However, when the UV laser beam passes through a smoke  
69 layer, the broadband fluorescence signal is induced and its spectrum includes the region of water  
70 vapor Raman lines. Thus, the signal in the water vapor channel (around 407.5 nm, when 354.7 nm  
71 laser radiation is emitted) becomes contaminated by the fluorescence backscatter signal (Immler et  
72 al., 2005; Immler and Schrems, 2005). This contamination can be reduced by decreasing the width  
73 of the transmission band in the water vapor channel down to tenths of nm. However, as it was  
74 shown recently, fluorescence still remains the source of uncertainties, especially when the water  
75 vapor mixing ratio (WVMR) is measured inside the smoke layers in the upper troposphere (Chouza  
76 et al., 2022; Reichardt et al., 2023).

77 Depolarization measurements provide an opportunity to monitor the presence of  
78 fluorescence signal in the Raman channel. The Q-branch of water vapor Raman lines (near 407.5  
79 nm) provides a weakly depolarized backscatter, while fluorescence is strongly depolarized. Thus,  
80 the presence of fluorescence should increase the depolarization ratio of signal in the water vapor  
81 channel. Moreover, if the depolarization ratios of water vapor and fluorescence are known, the  
82 contribution of fluorescence to the measured WVMR can be evaluated.

83 In this article, we report and analyze, for the first time, the depolarization ratio of aerosol  
84 fluorescence and of water vapor Raman backscatter from lidar observations performed at the  
85 ATOLL observatory (ATmospheric Observation at liLLe), Laboratoire d'Optique  
86 Atmosphérique, University of Lille, during dense smoke events occurred on May - June 2023. We  
87 start with a description of the experimental setup in Sect.2.1 and derive, in Sect. 2.2, the main  
88 equations for estimating the fluorescence contribution to the water vapor Raman channel. In the  
89 first part of the results section (Sect.3.1), the fluorescence depolarization ratios over ATOLL are  
90 analyzed for different aerosol types. The measurements of fluorescence spectra performed with a

91 new five-channel fluorescence lidar, operated in Moscow, are presented in Sect.3.2. In Sect. 3.3,  
92 we analyze the depolarization ratio in the water vapor Raman channel and estimate the  
93 contamination of fluorescence to the derived WVMR profiles. Finally, in Sect.4 we present our  
94 conclusions.

95

## 96 **2. Experimental setup and data analysis**

### 97 **2.1 Lidar system**

98 In our study, two lidar systems are considered. The first one, LILAS ((Lille Lidar  
99 AtmosphereS) is a multiwavelength Mie-Raman-Fluorescence lidar, whereas the second one is a  
100 multiwavelength fluorescence lidar operated by the General Physics Institute (GPI), Moscow  
101 (Veselovskii et al., 2023). Both systems are based on a tripled Nd:YAG laser (Q-Smart 450) with a  
102 20 Hz repetition rate and pulse energy about 100 mJ at 355 nm. The backscattered laser light in  
103 both systems is collected by a 40 cm aperture telescope and the lidar signals are digitized with  
104 transient recorders (Licel) with 7.5 m range resolution, allowing simultaneous detection in the  
105 analog and photon counting mode.

106 LILAS allows the so called  $3\beta+2\alpha+3\delta$  configuration, including three particle  
107 backscattering ( $\beta_{355}$ ,  $\beta_{532}$ ,  $\beta_{1064}$ ), two extinction ( $\alpha_{355}$ ,  $\alpha_{532}$ ) coefficients along with three particle  
108 depolarization ratios ( $\delta_{355}$ ,  $\delta_{532}$ ,  $\delta_{1064}$ ). The Raman channel with a 407.54/0.3 nm spectral width  
109 interference filter allows also water vapor profiling. At the end of 2019, the lidar was modified to  
110 enable fluorescence measurements. A part of the fluorescence spectrum is selected by a wideband  
111 interference filter of 44 nm width centered at 466 nm (Veselovskii et al. 2020).

112 In the fluorescence lidar of GPI only 355 nm wavelength is emitted, while fluorescence is  
113 measured in five spectral intervals. The central wavelengths and widths of spectral transmission  
114 bands (in parentheses) are: 438(29), 472(32), 513(29), 560(40) and 614(54) nm (Veselovskii et al.,  
115 2023). Thus, the fluorescence spectrum could be sampled at five different wavelengths. **The**  
116 **transmission bands of the fluorescence channels (Fig.1 in Veselovskii et al., 2023) are separated**  
117 **and there are no cross-talks between the channels.** At GPI, the measurements were performed at  
118 an angle of 48 deg to the horizon. The strong sunlight background restricts the fluorescence  
119 observations of both systems to only the nighttime hours.

120 Several aerosol properties can be derived from fluorescence. The fluorescence  
121 backscattering coefficient,  $\beta_{F\lambda}$ , at wavelength  $\lambda_F$ , is calculated from the ratio of fluorescence and

122 nitrogen Raman backscattering signals, as described in Veselovskii et al. (2020). We remind that  
 123  $\beta_{F\lambda}$  is related to fluorescence signals integrated over the filter transmission band  $D_\lambda$ . In Moscow  
 124 measurements are performed at five wavelengths, and to compare  $\beta_{F\lambda}$  between different channels  
 125 one makes use of the “fluorescence spectral backscattering coefficient”  $B_\lambda = \frac{\beta_{F\lambda}}{D_\lambda}$  (fluorescence  
 126 backscattering per spectral interval). LILAS has only one single fluorescence channel, therefore,  
 127 when presenting data from LILAS, for the sake of simplicity, one uses notation  $\beta_{F466} = \beta_F$ . The  
 128 intensive property characterizing aerosol fluorescence is the fluorescence capacity  $G_{F\lambda}$ , which is  
 129 the ratio of the fluorescence backscattering at wavelength  $\lambda_F$  to backscattering coefficient at laser  
 130 wavelength  $G_{F\lambda} = \frac{\beta_F}{\beta_\lambda}$ . This ratio, in principle, can be calculated for any laser wavelength. For  
 131 LILAS observations  $G_{F\lambda}$  is calculated with respect to  $\beta_{532}$ , as  $\beta_{532}$  is derived with rotational Raman  
 132 scattering and it does not depend on assumption about the Angstrom exponent (Veselovskii et al.  
 133 2015). And again, when presenting LILAS data, for simplicity one will use the notation  $G_{F\lambda} = G_F$ .  
 134 In this work, all profiles of aerosol properties are smoothed with the Savitzky – Golay method,  
 135 using second order polynomials with 8 points in the spatial window.

136 Additional information about the atmospheric thermodynamic state was available from  
 137 radiosonde measurements performed at Herstmonceux (UK) and Beauvechain (Belgium) stations,  
 138 located 160 km and 80 km away from the ATOLL observatory, respectively. When calculating the  
 139 relative humidity, one then used the water vapor profiles measured by Raman lidar and temperature  
 140 profiles provided by the radiosonde.

141 As discussed in Sect.1, measurements of fluorescence depolarization ratio and  
 142 depolarization of water vapor Raman backscatter are expected to bring new information about  
 143 aerosol properties and fluorescence contamination in the water vapor Raman channel. In 2023,  
 144 LILAS was upgraded to allow depolarization measurements at both 466 nm and 408 nm. The  
 145 corresponding optical layout is shown in Fig.1. Dichroic mirrors DM separate the 387, 408 and  
 146 466 nm components, while polarizing cubes split the components with polarizations oriented  
 147 parallel (s) and perpendicular (p) to the emitted polarized laser beam. For both channels, the  
 148 polarizing cube PBS251 from ThorLabs was used. The fluorescence depolarization ratio,  $\delta_F$ , and  
 149 the water vapor Raman scattering depolarisation ratio,  $\delta_W$ , are both defined and calculated as a  
 150 ratio of the perpendicular to the parallel respective components. The calibration of both ratios was

151 performed as described in Freudenthaler et al. (2009). The uncertainty of calibration is estimated  
 152 to be below 15% for both 466 and 408 nm channels.

153

## 154 ***2.2 Expressions for estimating fluorescence impact on water vapor measurements.***

155 As discussed in the recent work of Chouza et al. (2022) and Reichardt et al. (2023), the  
 156 broadband aerosol fluorescence is expected to contribute to the signal measured at the water vapor  
 157 Raman channel. Below, we provide the basic equations for estimating this contribution, based on  
 158 the measurements of the depolarization ratio in the water vapor Raman channel. The elastic  
 159 backscattered radiative power, at the laser wavelength  $\lambda_L$ , from distance  $z$ , can be modeled, after  
 160 background subtraction, by writing the lidar equation:

$$161 \quad P_L = O(z) \frac{1}{z^2} C_L \beta T_L^2 \quad (4)$$

162 where  $O(z)$  is the geometrical overlap factor, which is assumed to be the same for all channels.  $C_L$   
 163 is a range independent constant, including efficiency of the detection channel, the emitted laser  
 164 power and the receiving telescope diameter.  $T_L$  is the one-way atmospheric transmission,  
 165 describing light losses on the way from the lidar to distance  $z$  at wavelength  $\lambda_L$ .

$$166 \quad T_L = \exp \left\{ - \int_0^z [\alpha^a(\lambda_L, z') + \alpha^m(\lambda_L, z')] dz' \right\} \quad (5)$$

167 The backscattering and extinction coefficients contain the aerosol ( $a$ ) and molecular ( $m$ )  
 168 contributions:  $\beta_{\lambda_L} = \beta_{\lambda_L}^a + \beta_{\lambda_L}^m$  and  $\alpha_{\lambda_L} = \alpha_{\lambda_L}^a + \alpha_{\lambda_L}^m$ .

169 Radiative power in nitrogen Raman, water vapor Raman, and fluorescence channels can be  
 170 written in a similar way.

$$171 \quad P_R = O(z) \frac{1}{z^2} C_R \sigma_R N_R T_L T_R \quad (6)$$

$$172 \quad P_W = O(z) \frac{1}{z^2} C_W N_W \sigma_W T_W T_L \quad (7)$$

$$173 \quad P_F = O(z) \frac{1}{z^2} C_F \beta_F T_F T_L \quad (8)$$

174 where  $C_R$ ,  $C_W$ ,  $C_F$  are the corresponding range independent constants.  $T_R$ ,  $T_V$ , and  $T_F$  are the one-  
 175 way transmissions at wavelengths  $\lambda_R$ ,  $\lambda_W$ ,  $\lambda_F$ , corresponding to the centers of transmission bands of  
 176 the channels.  $N_R$  and  $N_W$  are the concentrations in nitrogen and water vapor molecules while  $\sigma_R$ ,

177  $\sigma_w$  are their Raman differential scattering cross sections respectively. The fluorescence  
 178 backscattering coefficient,  $\beta_F$ , is introduced the same way, as described in Veselovskii et al. (2020).

179 The received power of the fluorescence signal that leaks to the water vapor channel is:

$$180 \quad P_{FW} = O(z) \frac{1}{z^2} C_w \beta_{FW} T_w T_L \quad (9)$$

181 where  $\beta_{FW}$  is fluorescence backscattering coefficient at wavelength  $\lambda_w$ . The WVMR,  $n_w$ , can be  
 182 obtained from Eqs. 6 and 7, if the calibration constant  $K_w = \frac{C_R}{C_w} \frac{\sigma_R}{\sigma_w}$  is known:

$$183 \quad n_w = K_w \frac{P_w T_R}{P_R T_w} \quad (10)$$

184 The fluorescence backscattering coefficient,  $\beta_F$ , derived from Eq.6 and Eq.8, also contains  
 185 the calibration constant  $K_F$ . The procedure of calibration is described in Veselovskii et al. (2020).  
 186 Finally,  $\beta_F$  reads as:

$$187 \quad \beta_F = K_F n_R \frac{P_F T_R}{P_R T_F} \quad (11)$$

188 where  $n_R = \frac{N_R(z)}{N_R(z=0)}$  is the relative change of number density of nitrogen molecules with height.

189 The fluorescence signal  $P_{FW}$  in the water vapor channel can be expressed from  $P_F$  using parameter  
 190  $\eta$ , which depends on the ratio of fluorescence cross sections at wavelengths  $\lambda_w$  and  $\lambda_F$ , on the  
 191 filters width and on the efficiency of both channels, as follows:

$$192 \quad P_{FW} = P_F \eta \frac{T_w}{T_F} \quad (12)$$

193 The total signal measured in the water vapor channel,  $\tilde{P}_w$ , is the addition of both water vapor  
 194 backscatter,  $P_w$ , and the fluorescence backscatter,  $P_{FW}$ ,

$$195 \quad \tilde{P}_w = P_w + P_{FW} = P_w + P_F \eta \frac{T_w}{T_F} \quad (13)$$

196 One should remember, that the fluorescence spectrum, even for the same type of aerosols, can vary  
 197 with altitude and from observation to observation, which finally influences  $\eta$ . To minimize this  
 198 influence it is desirable to keep  $\lambda_w$  and  $\lambda_F$  as close as possible.

199 If the received lidar signals at the water vapor Raman and fluorescence channels are  
 200 separated into co-polarized ( $||$ ) and cross-polarized ( $\perp$ ) components, in respect to the polarization  
 201 of the emitted laser beam, their powers at the water vapor Raman channel are **given** respectively:

$$202 \quad \tilde{P}_W^{\square} = P_W^{\square} + P_F^{\square} \eta \frac{T_W}{T_F} \quad (14)$$

$$203 \quad \tilde{P}_W^{\perp} = P_W^{\perp} + P_F^{\perp} \eta \frac{T_W}{T_F} = \delta_W P_W^{\square} + \delta_F P_F^{\square} \eta \frac{T_W}{T_F} \quad (15)$$

204 where  $\delta_F$  and  $\delta_W$  are the fluorescence and water vapor Raman depolarization ratios, defined as:

$$205 \quad \delta_F = \frac{P_F^{\perp}}{P_F^{\square}} \quad \text{and} \quad \delta_W = \frac{P_W^{\perp}}{P_W^{\square}} \quad (16)$$

206 Here we assume that the depolarization ratio of fluorescence is the same at the wavelengths  $\lambda_W$   
 207 and  $\lambda_F$ . This assumption is usually valid, because fluorescence emission is normally from the  
 208 lowest singlet state, so the depolarization ratio is spectrally independent (Lakowicz, 2006).

209 Due to the presence of fluorescence, the depolarization ratio measured at the water vapor  
 210 Raman channel is:

$$211 \quad \tilde{\delta}_W = \frac{\tilde{P}_W^{\perp}}{\tilde{P}_W^{\square}} = \frac{\delta_W P_W^{\square} + \delta_F P_F^{\square} \eta \frac{T_W}{T_F}}{P_W^{\square} + P_F^{\square} \eta \frac{T_W}{T_F}} \quad (17)$$

212 Here  $\delta_W$  is the depolarization ratio that would be measured at the water vapor Raman channel in  
 213 the absence of atmospheric fluorescence. From Eqs.9, 10, 14, 15, 17 the parameter  $\eta$  can be derived  
 214 using the lidar measured values, such as the water vapor mixing ratio  $\tilde{n}_W$ , depolarization ratio  $\tilde{\delta}_W$ ,  
 215 and fluorescence backscattering,  $\beta_F$ :

$$216 \quad \eta = \frac{\tilde{n}_W K_F}{\beta_F K_W} n_R \frac{(1 + \delta_F)(\tilde{\delta}_W - \delta_W)}{(1 + \tilde{\delta}_W)(\delta_F - \delta_W)} \quad (18)$$

217 where  $\tilde{n}_W$  is the WVMR containing the fluorescence contribution.

218 It should be noted, that the choice of calibration constants  $K_F$ ,  $K_W$  does not influence  $\eta$ , because  
 219  $\tilde{n}_W$  and  $\beta_F$  are calculated using the same calibration constants. Finally, the increase of WVMR  
 220  $\Delta n_W$  induced by the fluorescence can be calculated as:



$$\Delta n_w = K_w \frac{P_F \eta \frac{T_w}{T_F} \frac{T_R}{T_w}}{P_R} = \frac{K_w}{K_F} \eta \beta_F \frac{1}{n_R} \quad (19)$$

As soon as the parameter  $\eta$  is calculated from Eq.18, we can estimate the relevant error  $\Delta n_w$  from  $\beta_F$ , which in the case of LILAS is measured at 466 nm (Veselovskii et al., 2020). In such estimation we have to assume that the relationship between fluorescence at 466 nm and 408 nm remains constant with height. A possibility to perform correction from single – channel fluorescence measurements was discussed by Reichardt et al. (2023), where it was shown, that for 466/408 nm channels, correction actually may depend on height. The corresponding analysis based on our measurements will be presented in Sect.3.2.

We should mention that when the depolarization at the water vapor Raman channel is available, the contribution of fluorescence to WVMR can be obtained without using  $\eta$ . From Eqs.18 and 19 we obtain:

$$\Delta n_w = \tilde{n}_w \frac{(1 + \delta_F)(\tilde{\delta}_w - \delta_w)}{(1 + \tilde{\delta}_w)(\delta_F - \delta_w)} \quad (20)$$

However, such correction can be performed only at low altitudes, where the signal-to-noise ratio at the cross-polarized water vapor channel is sufficient for calculation of  $\tilde{\delta}_w$ .

235

### 3. Experimental results

In May – June 2023, the Canadian forest fires were at the origin of numerous smoke layers observations in a wide range of altitude, ranging from the PBL to the tropopause. The Boreal wildfire season in 2023 started anomalously early. A wildfire in Alberta, Canada at 53.2° N, 115.7° W has produced an intense Pyrocumulonimbus (PyroCb) cloud on 5 May with the minimum satellite-derived infrared brightness temperature of -66° C, which should correspond to 10-11 km altitude according to local radiosoundings. In order to describe the long-range transport of the smoke plume produced by this event, we use UV absorbing Aerosol Index (AI) measurements by the Ozone Monitoring and Profiling Suite (OMPS) Nadir Mapper (NM) instrument onboard Suomi NPP satellite mission (Flynn et al., 2014). AI is widely used as a proxy of the amount of absorbing aerosols (e.g smoke, dust, ash) and its dimensionless value is proportional to the altitude of the aerosol layers. AI values above 15 are usually associated with smoke plumes at or above the

248 tropopause (Peterson et al., 2018 and references therein), whereas maximum AI value reported by  
249 the OMPS-NM instrument for the Alberta event reached to 19.9.

250 Fig. 2 displays the spatio-temporal evolution of the smoke plume from the Alberta event  
251 represented by the areas of enhanced AI observed between 5–21 May. The smoke in the upper  
252 troposphere and lower stratosphere (UTLS) is advected by the westerly winds, crossing the  
253 Atlantic about 1 week before reaching Moscow by 15 May. On that date, the Moscow lidar has  
254 detected the smoke layer at 10-11 km (see Sect.3.2). The plume was then further advected across  
255 Eurasia towards northeastern Siberia. By 22 May the smoke plume completes its first  
256 circumnavigation (not shown) and passes over Lille on 23 May and then over Moscow for the  
257 second time around 27 May. Thus, we can expect, that the smoke layers observed over Lille and  
258 Moscow have the same source.

259

### 260 *3.1 Variability of fluorescence depolarization ratio*

261 At the first stage of our research we focused on the variability of the fluorescence  
262 depolarization ratio for aerosol types. The main attention was paid to smoke particles, because  
263 they provide the strongest impact on the Raman water vapor measurements due to their high  
264 fluorescence capacity (Veselovskii et al., 2022).

265 Spatio-temporal distributions of the aerosol elastic and fluorescence backscattering  
266 coefficients ( $\beta_{532}$  and  $\beta_F$ ), on the night 26-27 June 2023, are shown in Fig.3. Dense smoke layer  
267 with  $\beta_F$  as high as  $7.0 \times 10^{-4} \text{ Mm}^{-1} \text{sr}^{-1}$  occurred within the 4.0-10.0 km height range. **The HYSPLIT**  
268 **back trajectories show that the air masses were transported from North America.** The relative  
269 humidity increased from 40% at 4 km to  $\text{RH} > 90\%$  at 7 km where formation of ice crystals started.  
270 Vertical profiles of aerosol elastic and fluorescence backscattering coefficients ( $\beta_{532}$  and  $\beta_F$ ),  
271 together with fluorescence capacity, are shown in Fig.3c. Inside the smoke layer,  $G_F$  is about  $3 \times 10^{-4}$ ,  
272 which is a typical value for smoke (Veselovskii et al., 2022) whereas, above 6 km, it decreases  
273 due to ice formation. The presence of ice crystals increased the particle depolarization ratio  $\delta_{532}$   
274 from 3% at 6 km to 20% at 8 km. Fluorescence signals are strongly depolarized. Inside the PBL,  
275  $\delta_F$  was about 60% whereas above 2 km it dropped to approximately 45%. The processes of  
276 hygroscopic growth and ice formation do not provide a noticeable impact on  $\delta_F$  value. During May  
277 – June observations, the depolarization ratio of smoke varied mainly inside the 45-55% range.

278 As discussed in our previous publications (Veselovskii, et al., 2022; Hu et al., 2022), the  
279 fluorescence capacity of aged smoke varies inside the  $(2.5-5.5)\times 10^{-4}$  range, probably due to the  
280 changes in smoke composition and conditions of atmospheric transport. However, during the  
281 Alberta fires, several smoke plumes with high  $G_F$  have been observed. The highest fluorescence  
282 capacity was observed on the night 16-17 June 2023. Vertical profiles of the aerosol properties for  
283 this episode are shown in Fig.4. Dense smoke layers with fluorescence backscattering exceeding  
284  $10.0\times 10^{-4} \text{ Mm}^{-1}\text{sr}^{-1}$  occurred within the 7.0 -9.0 km height range. In this case, the maximal value  
285 of the fluorescence capacity reached  $10.0\times 10^{-4}$ . Fluorescence depolarization ratio was measured  
286 about 50% through the entire smoke layer and the process of ice formation (just like in Fig.3d)  
287 does not influence  $\delta_F$ . Thus, in May - June 2023 strong variations of  $G_F$  in the  $(2.5-10.0)\times 10^{-4}$   
288 range were accompanied by relatively small variations of  $\delta_F$  remaining in the 45-55% interval.

289 It is known that in the UTLS smoke particles can reach depolarization ratio,  $\delta_{532}$ , as high as  
290 15-20% (Burton et al., 2015; Haarig et al., 2018; Hu et al., 2019; Baars et al., 2019; Ohneiser et  
291 al., 2020). High values of the **particle** depolarization ratio are usually attributed to the complex  
292 internal structure of smoke particles (Mishchenko et al., 2016). Two smoke events in the UTLS,  
293 characterized by enhanced  $\delta_{532}$ , on 28-29 May and 3-4 June 2023, are illustrated on Fig.5. On 28-  
294 29 May, three smoke layers, at  $\sim 3.5, 6.5$  and  $11.5$  km can be distinguished. High depolarization  
295 ratios, reaching 40% at altitudes of 9.8-10.5 km, are due to ice clouds. In the lower smoke plumes  
296 ranging between 3.5 and 6.5 km, the particle depolarization did not exceed 8%, whereas above 11  
297 km  $\delta_{532}$  increased to 15%. High values of  $\delta_{532}$  observed in the UTLS correlate with increase of  $G_F$   
298 and with fluorescence depolarization,  $\delta_F$ , up to  $7.0\times 10^{-4}$  and 70%, respectively. Similar behavior  
299 was observed on 3-4 June, where depolarization ratio,  $\delta_{532}$ , above 11.5 km increased up to 15%,  
300 simultaneously with an increase of  $G_F$  and  $\delta_F$  up to  $9.5\times 10^{-4}$  and 70% respectively. Thus, change  
301 in particle morphology may affect the depolarization ratio at the fluorescence channel. Another  
302 possibility is that, in the UTLS, not only the particle structure can change, but the composition as  
303 well. At the current stage of analysis, we are not yet able to conclude about the mechanisms  
304 explaining the increase of fluorescence depolarization in the UTLS.

305 Furthermore, we did not observe the effect of atmospheric humidity on smoke fluorescence  
306 depolarization. However, inside the PBL the observed hygroscopic growth was accompanied by  
307 an increase of  $\delta_F$ . During the 9-16 June 2023 period numerous particle hygroscopic growth cases  
308 were observed in the PBL. One of such cases, on the night of 12-13 June, is shown in Fig.6. The

309 relative humidity increased inside the PBL from 50% to 70% causing an increase of  $\beta_{532}$  near the  
310 PBL top. Depolarization ratio  $\delta_{532}$  decreased with height, since the particles in the process of  
311 hygroscopic growth became more spherical. The fluorescence depolarization ratio, however,  
312 increased inside the PBL from 50% to 70%.

313 All results obtained during 9-16 June, showing dependence of  $\delta_F$  and  $\delta_{532}$  on the relative  
314 humidity, are summarized in Fig.7. Particle depolarization  $\delta_{532}$  systematically decreased with RH  
315 but, on 16 June, this dependence is not monotonic which could be due to the change of aerosol  
316 composition with height. At low RH (below 30%), the fluorescence depolarization ratio was about  
317 50%. However, at RH about 90%,  $\delta_F$  increased up to 70%. One of possible explanations for that  
318 behavior could be an increase of rotational mobility of the molecules in the process of particle  
319 water uptake.

320

### 321 ***3.2 Fluorescence spectrum sampled with a with 5-channel lidar***

322 The results presented in the previous section were obtained with a single channel  
323 fluorescence lidar. However, for analyzing the variability of smoke properties (for example,  
324 increase of the fluorescence capacity with height) it is important to have information about a wider  
325 fluorescence spectrum. Moreover, to estimate the fluorescence contamination in the Raman water  
326 vapor channel, a relationship between fluorescence backscattering at 466 nm and 408 nm is used.  
327 Thus, we need to know the variability of the fluorescence spectrum in the short wavelength region.  
328 In our recent work (Veselovskii et al., 2023) we presented the first results obtained with a 5-  
329 channel fluorescence lidar in operation at the GPI. This lidar is able to measure the fluorescence  
330 backscattering profiles at 5 spectral intervals centered at 438, 472, 513, 560, and 614 nm. During  
331 May–June 2023, several smoke plumes originating from Alberta fires were transported over  
332 Moscow. Although Lille and Moscow are very distant from each other (above 2200 km), smoke  
333 plumes observed have the same origin, hence the fluorescence spectra measured over Moscow are  
334 quite helpful for the analysis of the Lille data.

335 Fig.8 (a,b,c) present the fluorescence spectral backscattering coefficients,  $B_\lambda$ , for 3 smoke  
336 events detected in the UTLS above 10, 8 and 10 km for 15, 31 May and 20 June 2023, respectively.  
337 On 15 and 31 May smoke layers were also present inside the 4-6 km range. Inside the PBL the  
338 strongest fluorescence was systematically detected at the 438 nm channel while, at higher altitudes,  
339 the maxima shifted to 560 nm. As follows from Figs.8d-f, the ratio  $B_{560}/B_{438}$  remained in the range

340 0.4 -0.7 inside the PBL, whereas this ratio increased above 2.0 in the UTLS. Thus, for smoke  
341 events the maxima of the fluorescence spectrum shifted with height towards longer wavelengths.  
342 The ratio  $B_{513}/\beta_{355}$  also increased with height and, above 10 km, it reached the values of  $1 \times 10^{-5}$   
343  $\text{nm}^{-1}$ . In the UTLS, the maximal fluorescence capacity,  $G_F$ , measured by LILAS at 466 nm (with  
344 44 nm bandwidth filter) was about  $10 \times 10^{-4}$ . In the smoke layer, the ratio of backscattering  
345 coefficients  $\beta_{355}/\beta_{532}$  is about 2, so the maximal ratio  $B_{466}/\beta_{355}$  derived from LILAS measurements  
346 was about  $1.1 \times 10^{-5} \text{ nm}^{-1}$ . Thus, values obtained over Lille and over Moscow are in good  
347 agreement.

348 The fluorescence spectra obtained for the above mentioned smoke plumes are shown in  
349 Fig.9. The values of  $B_\lambda$  are normalized to  $B_{438}$ . Inside the PBL, the maximum of fluorescence was  
350 measured at 438 nm and it decreased with wavelength. In the smoke layers within 4-6 km, the  
351 maximum of fluorescence is observed at 513 nm while, in the UTLS, the maximum shifted to 560  
352 nm.

353 When applying Eq.19 to estimate the contribution of smoke fluorescence into the Raman  
354 water vapor channel of LILAS, we assumed that the ratio of the fluorescence backscattering at  
355 466 nm to 408 nm ( $B_{466}/B_{408}$ ), was constant. For the lidar in operation at GPI, the shortest available  
356 wavelength was 438 nm, therefore, at least, one can estimate the variability of the ratio  $B_{472}/B_{438}$ .  
357 Fig. 10 presents the vertical profiles of  $B_{472}/B_{438}$  for 11 smoke events occurring during the 15 May-  
358 20 June 2023 period. Inside the PBL, this ratio varied in the 0.6–1.0 range. The lowest values  
359 correspond to urban aerosols while, values of  $B_{472}/B_{438}$  close to 1.0, probably indicate the presence  
360 of smoke particles inside the PBL. Smoke layers were observed mainly above 4.0 km and  $B_{472}/B_{438}$   
361 showed a tendency to increase in the UT. It is interesting that, for the period 15 May–1 June, the  
362 ratio was close to 1.5 whereas after 1 June, it became close to 1.0, which can be related to changing  
363 of smoke source. Mean value of  $B_{472}/B_{438}$  in the 4.0–11.0 km range over all observations is 1.38  
364 with standard deviation of 0.23 (relative variation is about 17%). For the channels 466 nm and 408  
365 nm the wavelength separation is larger, so one can expect a variation of  $B_{466}/B_{408}$  in the smoke  
366 layer to be above that value. It points out the difficulties to face when the estimation of the  
367 fluorescence contamination to the Raman water vapor channel is performed from a single  
368 fluorescence channel at 466 nm. This issue was also discussed by Reichardt et al. (2023).

369

### 370 ***3.3 Estimation of fluorescence impact on water vapor Raman measurements***

371 Measuring the depolarization ratio at the water vapor Raman channel provides an  
 372 opportunity to control/evaluate the presence of fluorescence leak in this channel. These  
 373 depolarization measurements were performed over Lille during May – June 2023. Vertical profiles  
 374 of water vapor depolarization ratio  $\tilde{\delta}_w$  together with  $\tilde{n}_w$ ,  $\beta_{532}$ ,  $\beta_F$ , and  $G_F$  are shown in Fig.11 for  
 375 the night 8-9 June and 10-11 June 2023. On 8-9 June the aerosols were confined mainly below 5  
 376 km. The fluorescence capacity was about  $1.0 \times 10^{-4}$  below 3.0 km, but above,  $G_F$  increased up to  
 377  $2.5 \times 10^{-4}$ , indicating to the presence of smoke particles. The depolarization ratio in the water vapor  
 378 channel was about 2% in the height range 1.5–3.5 km, where the values of  $\tilde{\delta}_w$  ranging within 1.8-  
 379 2.0% were observed at this height range, where the contribution of fluorescence was insignificant.  
 380 The depolarization ratio  $\delta_w$  was low, because the interference filter at the water vapor channel  
 381 selects only strongest Q-branch lines and most of rotational lines are blocked. The contribution of  
 382 fluorescence becomes noticeable above 3.5 km where  $n_w$  dropped, resulting in an increase of  $\tilde{\delta}_w$   
 383 up to ~3%. Below 1 km height we also observed an increase of  $\tilde{\delta}_w$  up to 2.2%, where fluorescence  
 384 backscattering is enhanced. Similar values of  $\tilde{\delta}_w$  were observed on 10-11 June, where the  
 385 depolarization ratio increased up to 2.5% inside the smoke layer observed at ~3.75 km and below  
 386 2.0 km.

387 As discussed in Sect. 2.2, the contribution of fluorescence to the WVMR channel can be  
 388 derived from Eq.20 if  $\tilde{\delta}_w$  and  $\delta_F$  are measured simultaneously. Fig.12 presents the modeling of  
 389 the relative error  $\frac{\Delta n_w}{\tilde{n}_w}$ , introduced by the fluorescence to the WVMR channel as a function of  $\tilde{\delta}_w$ .  
 390 The computations are performed for different fluorescence depolarization ratios  $\delta_F=50\%$ , 60%,  
 391 70% to include both smoke and urban particles. A depolarization ratio in the Raman water vapor  
 392 channel in the absence of fluorescence was assumed to be  $\delta_w=2\%$ . For a depolarization ratio  $\tilde{\delta}_w$   
 393 below 3% the relative error  $\frac{\Delta n_w}{\tilde{n}_w}$  did not exceed 3%. As follows from the fluorescence spectra in  
 394 Fig.9, the fluorescence of urban particles increases towards shorter wavelengths, thus one can  
 395 expect an impact of the urban aerosol fluorescence on the water vapor measurements. In practice,  
 396 however, we did not observe values of  $\tilde{\delta}_w$  exceeding 3% in the PBL, thus, contribution of aerosol

397 in the PBL is not critical. The reason is due to the low fluorescence capacity (about one order lower  
398 than that of smoke) and higher water vapor content, comparing to the free troposphere.

399 Vertical profiles of  $\tilde{\delta}_w$  shown in Fig.11 become noisy at heights where  $n_w$  is low, and thus  
400  $\tilde{\delta}_w$  cannot be used for correction of the fluorescence effect in the upper troposphere. To overcome  
401 this, we derived the parameter  $\eta$  from Eq.18 at low altitudes where  $\tilde{\delta}_w$  values are available, and,  
402 thus, these  $\eta$  values can be used to calculate  $\Delta n_w$  from Eq.19 in the entire height range. In such an  
403 approach, however, one has to assume that the relationship between fluorescence cross sections at  
404 466 nm and 408 nm remains constant with height. As discussed in Sect. 3.2, such assumption can  
405 yield significant bias in the calculation of  $\Delta n_w$ , and, at this stage, we do not provide corrected  
406 profiles of the WVMR.

407 For the accurate calculation of  $\eta$  one needs smoke events with strongly enhanced  $\tilde{\delta}_w$  values,  
408 which are usually observed in the smoke layers with low WVMR. Such suitable events are shown  
409 on the nights of 26-27 May and 5-6 June 2023 in Fig.13. On 26-27 May a smoke layer  
410 characterized by high fluorescence ( $\beta_F$  up to  $5 \times 10^{-4} \text{ Mm}^{-1} \text{sr}^{-1}$ ) and low  $\tilde{n}_w$  (below 0.2 g/kg) values  
411 is observed at 3.5 km. The relevant fluorescence depolarization ratio was about 47% and  $\tilde{\delta}_w$   
412 increased from 2% up to 12% in the middle of this layer. The parameter  $\eta$  calculated from Eq.18  
413 inside this smoke layer was about  $2 \times 10^{-3} \text{ (g/kg)/(Mm}^{-1} \text{sr}^{-1})$ . On 5-6 June the depolarization ratio  
414  $\tilde{\delta}_w$  in the smoke layer increased up to 10% and value of  $\eta$  was very similar. The values of  $\eta$  derived  
415 for several smoke episodes varied in the range  $(2-2.5) \times 10^{-3} \text{ (g/kg)/(Mm}^{-1} \text{sr}^{-1})$ . For the estimate of  
416  $\Delta n_w$  we used the mean value of  $\eta = 2.25 \times 10^{-3} \text{ (g/kg)/(Mm}^{-1} \text{sr}^{-1})$ , which is suitable only for smoke,  
417 while for particles in the PBL,  $\eta$  can have a different value. However, in the PBL, the low  
418 depolarization ratios of  $\tilde{\delta}_w$  prevented us from calculating  $\eta$ .

419 Fig.14 presents the vertical profiles of WVMR, the fluorescence backscattering and the error  
420  $\Delta n_w$  introduced by the fluorescence in WVMR on 26-27 May, 28-29 May and 16-17 June. Smoke  
421 layers with strong fluorescence occurred systematically in our upper tropospheric observations.  
422 The current LILAS system is not powerful enough for deriving accurate water vapor measurements  
423 above 10 km, however an increase of  $\tilde{n}_w$  in the fluorescent smoke layers is visible. We remind that

424 Eq.19 for  $\Delta n_W$  contains the factor  $\frac{1}{n_R}$  (inverse relative change of nitrogen number density), thus,  
425 the fluorescence impact on WVMR will increase with height. The uncertainties  $\frac{\Delta n_W}{\tilde{n}_W}$  for all events  
426 considered are shown in Fig.14d. On 26-27 May and 28-29 May the uncertainty of  $\frac{\Delta n_W}{\tilde{n}_W}$  at 11 km  
427 is of the order of 100%. On 16 June the smoke layer is lower (at 9 km) and the uncertainty is about  
428 50%. Our demonstration shows that smoke fluorescence can significantly impact the water vapor  
429 measurements. The proposed approach, based on the analysis of the depolarization ratio of the  
430 water vapor signal, has the potential for estimation and correction of this impact.

#### 431 4. Conclusion

432 This study is one of the first efforts to measure the depolarization ratio of fluorescence of  
433 the atmospheric aerosols. Analysis of more than 30 spring and summer smoke events allows  
434 evaluation of the main aerosol intensive properties, including fluorescence capacity, particle and  
435 fluorescence depolarization ratio. The fluorescence capacity of smoke in the troposphere varied  
436 within  $(2.5-10.0)\times 10^{-4}$ , however, in spite of strong  $G_F$  variation,  $\delta_F$  was remaining within a  
437 relatively narrow interval 45-55%. Additional observations revealed that for smoke plumes in the  
438 upper troposphere the fluorescence depolarization ratio increased up to 70%. At the moment, we  
439 cannot fully explain the mechanism responsible for this  $\delta_F$  increase. It can be related to complex  
440 particle internal structure at high altitudes, as well as to the change of the chemical composition,  
441 revealed by the shift of the maximum of the fluorescence spectra to longer wavelengths in the  
442 upper troposphere (Fig. 9).

443 Inside the PBL, the fluorescence depolarization ratio was higher than that of smoke and  
444 varied within the 50-70% range. Moreover, the fluorescence depolarization ratio of urban particles  
445 strongly depends on the relative humidity and, in contrast to the elastic scattering, the  
446 depolarization of fluorescence increases with RH. One possible origin of this phenomena could be  
447 attributed to an increase of the rotational mobility of the molecules involved in the process of water  
448 uptake.

449 The depolarization ratio of the Raman water vapor backscatter, in the absence of  
450 fluorescence, appeared to be quite low ( $\delta_w=2\pm 0.5\%$ ). As a result, the depolarization ratio of the  
451 Raman water vapor backscatter is sensitive to the presence of strongly depolarized fluorescence



452 signals, and the contribution of fluorescence to the WVMR can be calculated from the measured  
453 value  $\tilde{\delta}_w$ . However, with the lidar used in this work, measurements of  $\tilde{\delta}_w$  are only possible up to  
454 the middle troposphere, while the problem of the fluorescence interference is the most crucial in  
455 UTLS. To estimate the impact of fluorescence on the WVMR in UTLS, the height independent  
456 parameter  $\eta$ , linking fluorescence at 466 nm and at 408 nm, was used. Such an approach relies on  
457 the assumption that  $\eta$  remains constant and allows only a rough estimation of the correction term  
458 for the WVMR,  $\Delta n_w$ . One possible solution to increase the accuracy of  $\Delta n_w$  is to implement an  
459 additional shorter wavelength channel (438 nm or even shorter). Another technical solution could  
460 be considered as the depolarization ratio of Raman water vapor backscatter is low, therefore the  
461 408 nm channel can be efficiently equipped with a polarizing cube. Thus, the depolarized channel  
462 at 408 nm can be used for fluorescence measurements. As the polarizing cubes work in a wide  
463 spectral range, so one can select the region outside of the water vapor spectrum (400–418 nm) for  
464 fluorescence monitoring. We plan this experiment as well as other innovative approaches with our  
465 future high-power fluorescence lidar, LIFE (Laser Induced Fluorescence Explorer), whose start of  
466 operation is scheduled for the beginning of 2024.

467

468 **Data availability.** Lidar measurements are available upon request  
469 (philippe.goloub@univ-lille.fr).

470

471 **Author contributions.** IV processed the data and wrote the paper. QH and TP performed the  
472 measurements in Lille. PG supervised the project and helped with paper preparation. WB modified  
473 LILAS for polarization measurements. MK and NK performed the measurements in Moscow. SK  
474 analyzed transport of smoke layers and RM derived RH profiles from lidar measurements.

475 .

476 **Competing interests.** The authors declare that they have no conflict of interests.

477

## 478 **Acknowledgement**

479 We acknowledge funding from the CaPPA project funded by the ANR through the PIA under  
480 contract ANR-11-LABX-0005-01, the “Hauts de France” Regional Council (project ECRIN) and  
481 the European Regional Development Fund (FEDER). ESA/QA4EO program is greatly  
482 acknowledged for supporting the observation activity at LOA. The work from Q. Hu was  
483 supported by Agence *Nationale* de Recherche ANR (*ANR-21-ESRE-0013*) through the  
484 OBS4CLIM project. Development of fluorescence lidar in Moscow was supported by Russian

485 Science Foundation (project 21-17-00114). The work of S. Khaykin was partly supported by the  
486 Agence Nationale de la Recherche (ANR) 21-CE01- 335 0007-01 PyroStrat project.

487

488 **References**

489

- 490 Baars, H., Ansmann, A., Ohneiser, K., Haarig, M., Engelmann, R., Althausen, D., Hanssen, I.,  
491 Gausa, M., Pietruczuk, A., Szkop, A., Stachlewska, I. S., Wang, D., Reichardt, J., Skupin, A.,  
492 Mattis, I., Trickl, T., Vogelmann, H., Navas-Guzmán, F., Haeferle, A., Acheson, K., Ruth, A.  
493 A., Tatarov, B., Müller, D., Hu, Q., Podvin, T., Goloub, P., Veselovskii, I., Pietras, C.,  
494 Haeffelin, M., Fréville, P., Sicard, M., Comerón, A., Fernández García, A. J., Molero  
495 Menéndez, F., Córdoba-Jabonero, C., Guerrero-Rascado, J. L., Alados-Arboledas, L., Bortoli,  
496 D., Costa, M. J., Dionisi, D., Liberti, G. L., Wang, X., Sannino, A., Papagiannopoulos, N.,  
497 Boselli, A., Mona, L., D'Amico, G., Romano, S., Perrone, M. R., Belegante, L., Nicolae, D.,  
498 Grigorov, I., Gialitaki, A., Amiridis, V., Soupiona, O., Papayannis, A., Mamouri, R.-E.,  
499 Nisantzi, A., Heese, B., Hofer, J., Schechner, Y. Y., Wandinger, U., and Pappalardo, G.: The  
500 unprecedented 2017–2018 stratospheric smoke event: decay phase and aerosol properties  
501 observed with the EARLINET, *Atmos. Chem. Phys.*, 19, 15183–15198,  
502 <https://doi.org/10.5194/acp-19-15183-2019>, 2019.
- 503 Burton, S.P., Hair, J.W., Kahnert, M., Ferrare, R.A., Hostetler, C.A., Cook, A.L., Harper, D.B.,  
504 Berkoff, T.A., Seaman, S.T., Collins, J.E., Fenn, M.A., and Rogers, R.R.: Observations of the  
505 spectral dependence of linear particle depolarization ratio of aerosols using NASA Langley  
506 airborne High Spectral Resolution Lidar, *Atmos. Chem. Phys.*, 15, 13453–13473,  
507 <https://doi.org/10.5194/acp-15-13453-2015>, 2015.
- 508 Chouza, F., Leblanc, T., Brewer, M., Wang, P., Martucci, G., Haeferle, A., Vérémes, H., Duflot,  
509 V., Payen, G., and Keckhut, P.: The impact of aerosol fluorescence on long-term water vapor  
510 monitoring by Raman lidar and evaluation of a potential correction method, *Atmos. Meas.*  
511 *Tech.*, 15, 4241–4256, <https://doi.org/10.5194/amt-15-4241-2022>, 2022.
- 512 Flynn, L., Long, C., Wu, X., Evans, R., Beck, C. T., Petropavlovskikh, I., McConville, G.,  
513 Yu, W., Zhang, Z., Niu, J., Beach, E., Hao, Y., Pan, C., Sen, B., Novicki, M., Zhou, S., Seftor,  
514 C.: Performance of the Ozone Mapping and Profiler Suite (OMPS) products, *J. Geophys. Res.*  
515 *Atmos.*, 119, 6181–6195, 2014. doi:10.1002/2013JD020467

516 Freudenthaler, V., Esselborn, M., Wiegner, M., Heese, B., Tesche, M. and co-authors:  
517 Depolarization ratio profiling at several wavelengths in pure Saharan dust during SAMUM  
518 2006, *Tellus* 61B, 165–179, 2009.

519 Haarig, M., Ansmann, A., Baars, H., Jimenez, C., Veselovskii, I., Engelmann, R., and Althausen,  
520 D.: Depolarization and lidar ratios at 355, 532, and 1064 nm and microphysical properties of  
521 aged tropospheric and stratospheric Canadian wildfire smoke, *Atmos. Chem. Phys.*, 18, 11847-  
522 11861, <https://doi.org/10.5194/acp-18-11847-2018>, 2018.

523 Hu, Q., Goloub, P., Veselovskii, I., Bravo-Aranda, J.-A., Popovici, I. E., Podvin, T., Haeffelin,  
524 M., Lopatin, A., Dubovik, O., Pietras, C., Huang, X., Torres, B., and Chen, C.: Long-range-  
525 transported Canadian smoke plumes in the lower stratosphere over northern France, *Atmos.*  
526 *Chem. Phys.*, 19, 1173-1193, 2019. <https://doi.org/10.5194/acp-19-1173-2019>.

527 Hu, Q., Goloub, P., Veselovskii, I., and Podvin, T.: The characterization of long-range transported  
528 North American biomass burning plumes: what can a multi-wavelength Mie-Raman-  
529 polarization-fluorescence lidar provide? *Atmos. Chem. Phys.* 22, 5399–5414, 2022  
530 <https://doi.org/10.5194/acp-22-5399-2022>

531 Immler, F. and Schrems, O.: Is fluorescence of biogenic aerosols an issue for Raman lidar  
532 measurements? *Proc. SPIE* 5984, Lidar Technologies, Techniques, and Measurements for  
533 Atmospheric Remote Sensing, 59840H, <https://doi.org/10.1117/12.628959>, 2005.

534 Immler, F., Engelbart, D., and Schrems, O.: Fluorescence from atmospheric aerosol detected by a  
535 lidar indicates biogenic particles in the lowermost stratosphere, *Atmos. Chem. Phys.*, 5, 345–  
536 355, <https://doi.org/10.5194/acp-5-345-2005>, 2005.

537 Lakowicz, J. R.: Principles of Fluorescence Spectroscopy, Springer New York, NY, 2006.  
538 <https://doi.org/10.1007/978-0-387-46312-4>

539 Liu, F., Yi, F., He, Y., Yin, Z., Zhang, Y., and Yu, C.: Spectrally Resolved Raman Lidar to  
540 Measure Backscatter Spectra of Atmospheric Three-Phase Water and Fluorescent Aerosols  
541 Simultaneously: Instrument, Methodology, and Preliminary Results, *IEEE Transactions on*  
542 *Geoscience and Remote Sensing*, 60, 5703013, 2022, doi: 10.1109/TGRS.2022.3166191

543 Mishchenko MI, Dlugach JM, Liu L. Linear depolarization of lidar returns by aged smoke  
544 particles. *Appl Opt.* 55, 9968-9973, doi: 10.1364/AO.55.009968, 2016.

545 Ohneiser, K., Ansmann, A., Baars, H., Seifert, P., Barja, B., Jimenez, C., Radenz, M., Teisseire,  
546 A., Floutsi, A., Haarig, M., Foth, A., Chudnovsky, A., Engelmann, R., Zamorano, F., Bühl,

547 J., and Wandinger, U.: Smoke of extreme Australian bushfires observed in the stratosphere  
548 over Punta Arenas, Chile, in January 2020: optical thickness, lidar ratios, and depolarization  
549 ratios at 355 and 532 nm, *Atmos. Chem. Phys.*, 20, 8003–8015, [https://doi.org/10.5194/acp-](https://doi.org/10.5194/acp-20-8003-2020)  
550 [20-8003-2020](https://doi.org/10.5194/acp-20-8003-2020), 2020.

551 Peterson, D.A., Campbell, J.R., Hyer, E.J. et al. Wildfire-driven thunderstorms cause a volcano-  
552 like stratospheric injection of smoke, *npj Clim. Atmos. Sci.* 1, 30, 2018.  
553 <https://doi.org/10.1038/s41612-018-0039-3>

554 Rao, Z., He, T., Hua D, Wang, Y., Wang, X., Chen, Y., Le J.: Preliminary measurements of  
555 fluorescent aerosol number concentrations using a laser-induced fluorescence lidar, *Appl. Opt.*  
556 *57*, 7211-7215, <https://doi.org/10.1364/AO.57.007211>, 2018.

557 Reichardt, J.: Cloud and aerosol spectroscopy with Raman lidar, *J. Atmos. Ocean. Tech.*, 31,  
558 1946–1963, <https://doi.org/10.1175/JTECH-D-13-00188.1>, 2014.

559 Reichardt, J., Leinweber, R., Schwebe, A.: Fluorescing aerosols and clouds: investigations of co-  
560 existence, *EPJ Web Conf.*, 176, 05010, <https://doi.org/10.1051/epjconf/201817605010>, 2018.

561 Reichardt, J., Behrendt, O., and Lauer mann, F.: Spectrometric fluorescence and Raman lidar:  
562 absolute calibration of aerosol fluorescence spectra and fluorescence correction of humidity  
563 measurements, *Atmos. Meas. Tech.*, 16, 1–13, 2023. <https://doi.org/10.5194/amt-16-1-2023>.

564 Richardson, S.C., Mytilinaios, M., Foskinis, R., Kyrou, C., Papayannis, A., Pyrri, I., Giannoutsou,  
565 E., Adamakis, I.D.S.: Bioaerosol detection over Athens, Greece using the laser induced  
566 fluorescence technique, *Science of the Total Environment* 696, 133906, 2019.  
567 <https://doi.org/10.1016/j.scitotenv.2019.133906>

568 Sugimoto, N., Huang, Z., Nishizawa, T., Matsui, I., Tatarov, B.: Fluorescence from atmospheric  
569 aerosols observed with a multichannel lidar spectrometer," *Opt. Expr.* 20, 20800-20807,  
570 <https://doi.org/10.1364/OE.20.020800>, 2012.

571 Veselovskii, I., Whiteman, D. N., Korenskiy, M., Suvorina, A., and Pérez-Ramírez, D.: Use of  
572 rotational Raman measurements in multiwavelength aerosol lidar for evaluation of particle  
573 backscattering and extinction, *Atmos. Meas. Tech.*, 8, 4111–4122,  
574 <https://doi.org/10.5194/amt-8-4111-2015>, 2015.

575 Veselovskii, I., Hu, Q., Goloub, P., Podvin, T., Korenskiy, M., Pujol, O., Dubovik, O., Lopatin,  
576 A.: Combined use of Mie-Raman and fluorescence lidar observations for improving aerosol

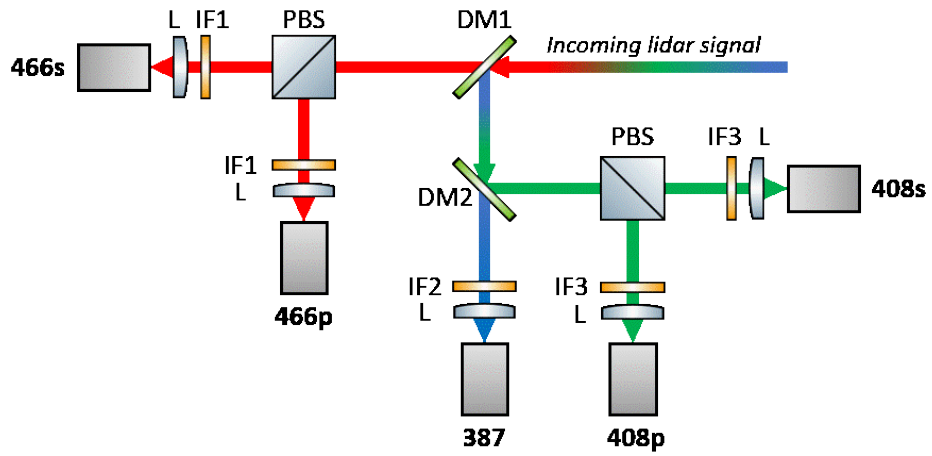
577 characterization: feasibility experiment, *Atm. Meas. Tech.*, 13, 6691–6701, 2020.  
578 [doi.org/10.5194/amt-13-6691-2020](https://doi.org/10.5194/amt-13-6691-2020).

579 Veselovskii, I., Hu, Q., Goloub, P., Podvin, T., Barchunov, B., and Korenskii, M.: Combining  
580 Mie–Raman and fluorescence observations: a step forward in aerosol classification with lidar  
581 technology, *Atmos. Meas. Tech.*, 15, 4881–4900, 2022. [https://doi.org/10.5194/amt-15-4881-](https://doi.org/10.5194/amt-15-4881-2022)  
582 [2022](https://doi.org/10.5194/amt-15-4881-2022).

583 Veselovskii, I., Kasianik, N., Korenskii, M., Hu, Q., Goloub, P., Podvin, T., and Liu, D.:  
584 Multiwavelength fluorescence lidar observations of smoke plumes, *Atmos. Meas. Tech.*, 16,  
585 2055–2065, 2023. <https://doi.org/10.5194/amt-16-2055-2023>

586 Whiteman, D. N.: Examination of the traditional Raman lidar technique. I. Evaluating the  
587 temperature dependent lidar equations, *Appl. Optics*, 42, 2571–2592,  
588 <https://doi.org/10.1364/AO.42.002571>, 2003.  
589

590



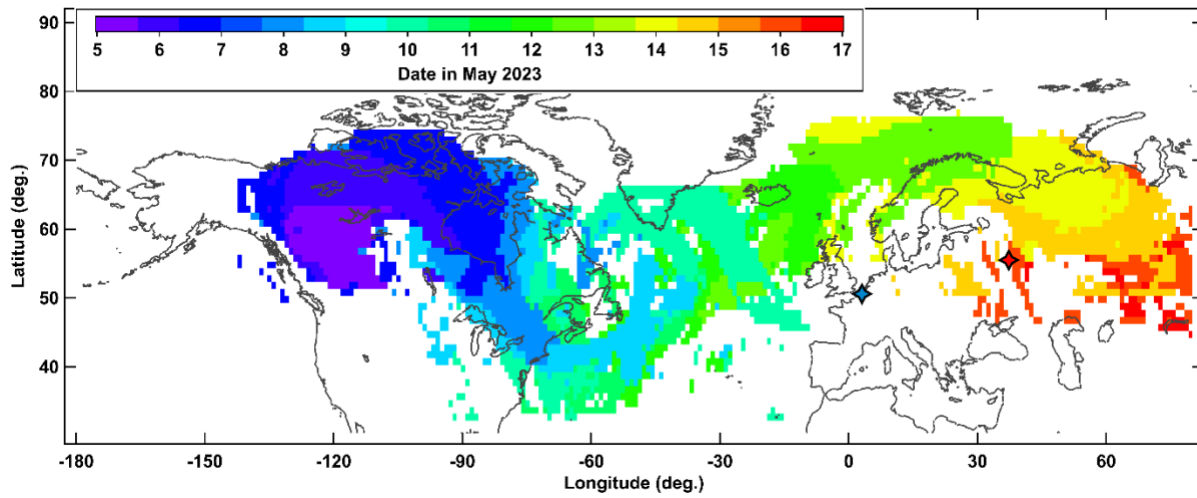
591

592 Fig.1. Optical layout of depolarization measurements at 408 nm and 466 nm wavelengths. L –  
593 lens; IF1- IF3 – interference filters, DM1, DM2 – dichroic mirrors, PBS – polarizing cube.

594

595

596



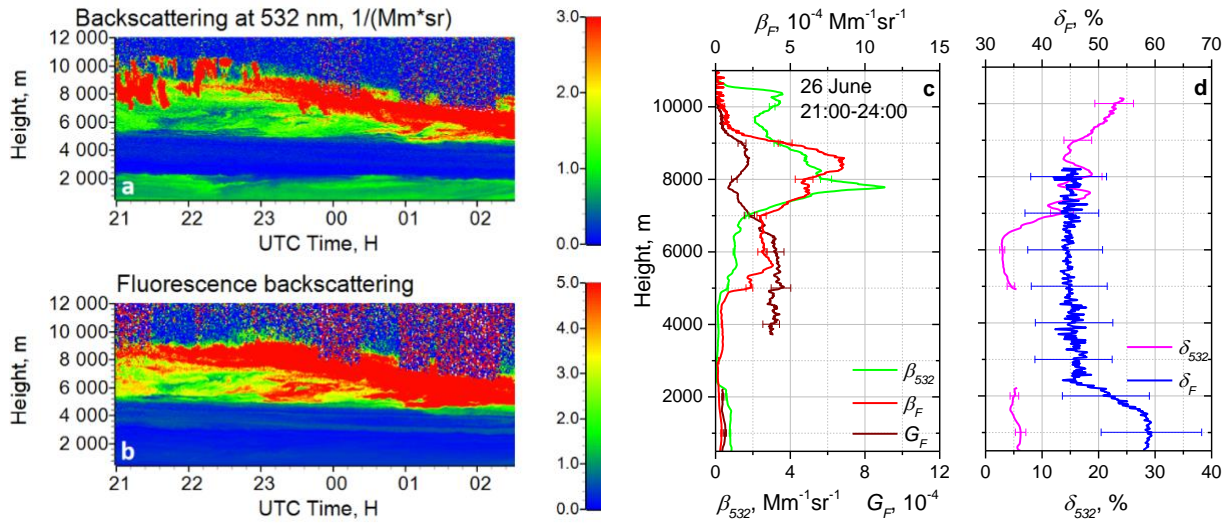
597

598 Fig.2. Spatio-temporal evolution of the smoke plume from the wildfire event in Alberta, Canada  
599 on 5 May 2023. Color-filled time-coded areas indicate the Aerosol Index (AI) values from the  
600 OMPS-NPP instrument exceeding 0.5. The blue and red-filled stars indicate the location of Lille  
601 and Moscow lidar stations, respectively.

602

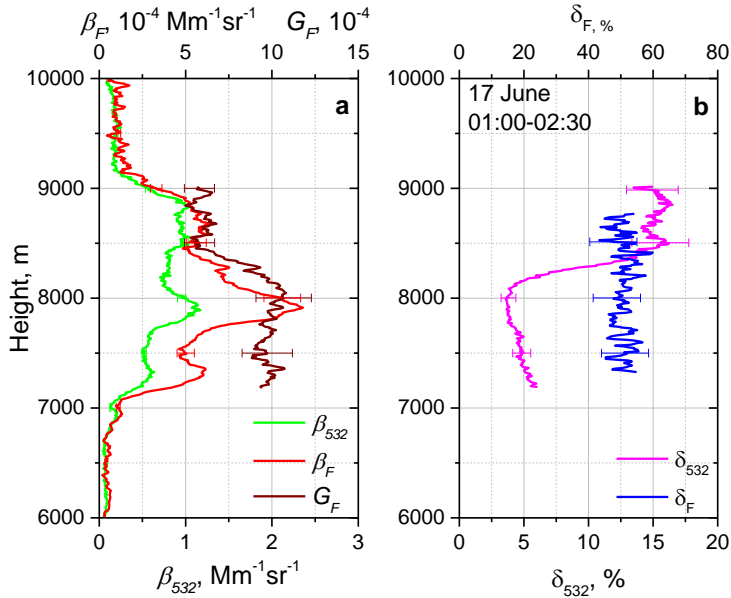


603  
604



605  
606 Fig.3. Smoke event on the night 26-27 June 2023 over Lille. Spatio-temporal distributions of (a)  
607 aerosol backscattering coefficient  $\beta_{532}$  and (b) fluorescence backscattering  $\beta_F$  (in  $10^{-4} \text{ Mm}^{-1}\text{sr}^{-1}$ ).  
608 Vertical profiles of (c) the aerosol  $\beta_{532}$  and fluorescence  $\beta_F$  backscattering coefficients, the  
609 fluorescence capacity  $G_F$ ; (d) the particle  $\delta_{532}$  and the fluorescence  $\delta_F$  depolarization ratios.

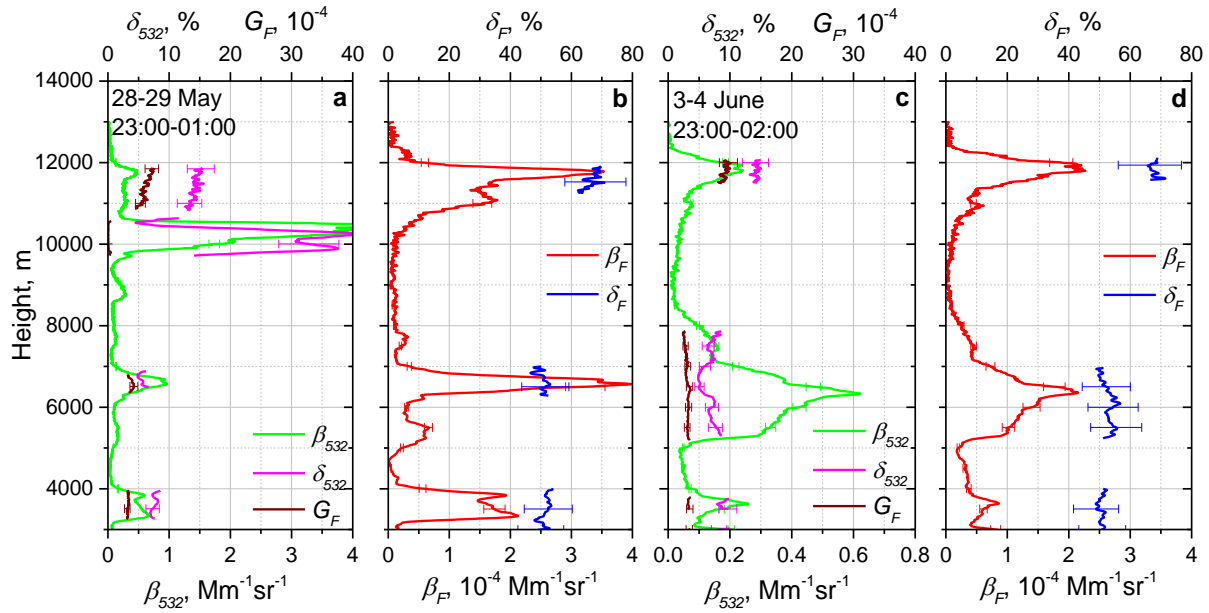
610  
611



612  
613 Fig.4. Vertical profiles of (a) aerosol  $\beta_{532}$  and fluorescence  $\beta_F$  backscattering coefficients,  
614 fluorescence capacity  $G_F$  and (b) particle  $\delta_{532}$  and fluorescence  $\delta_F$  depolarization ratios on the night  
615 16-17 June 2023 for period 01:00-02:30 UTC over Lille.

616  
617

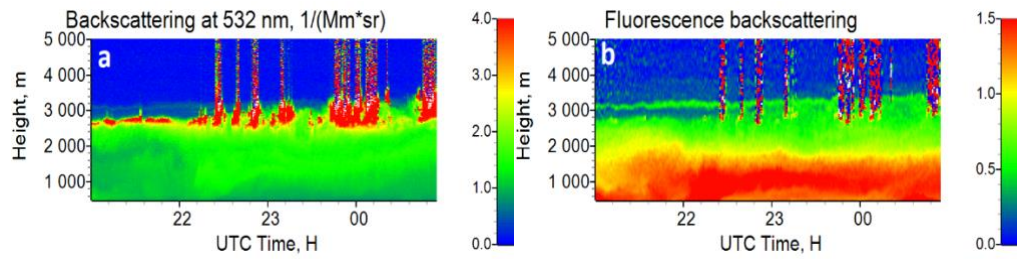
618  
619



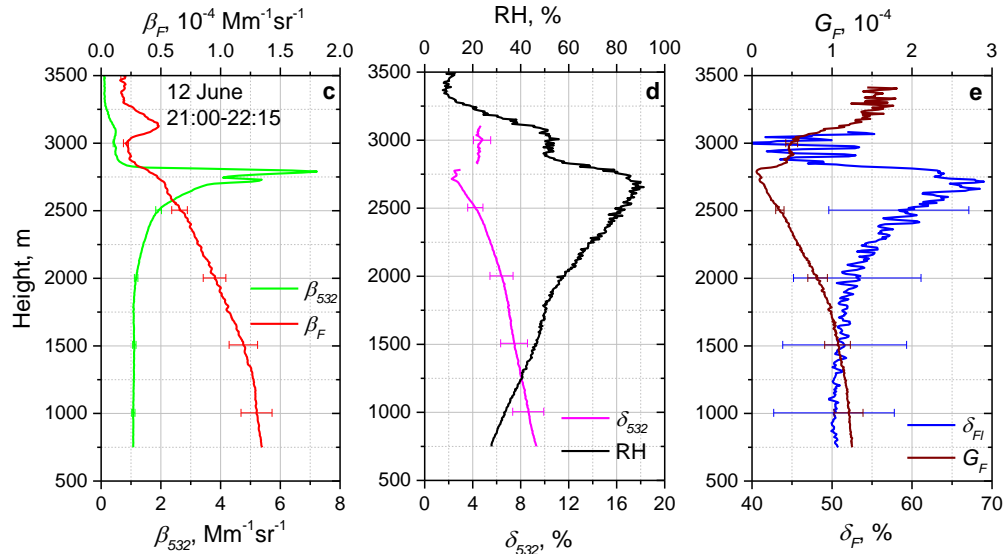
620  
621  
622  
623  
624  
625

Fig.5. Vertical profiles of (a, c) backscattering coefficient  $\beta_{532}$ , particle depolarization ratio  $\delta_{532}$ , fluorescence capacity  $G_F$  and (b, d) fluorescence backscattering  $\beta_F$  and fluorescence depolarization ratio  $\delta_F$  for two smoke episodes on the nights 28-29 May 2023 and 3-4 June 2023 over Lille.

626



627



628

629

630

631

632

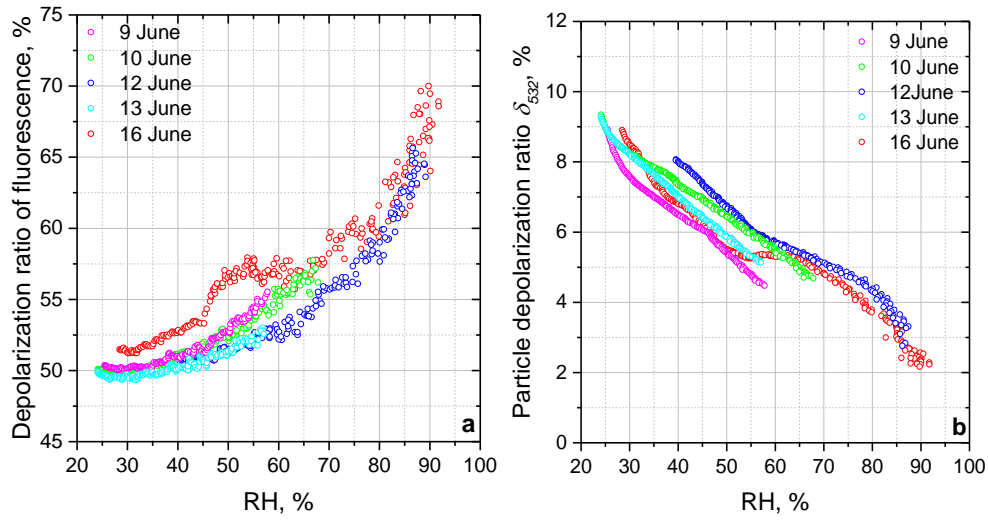
633

634

635

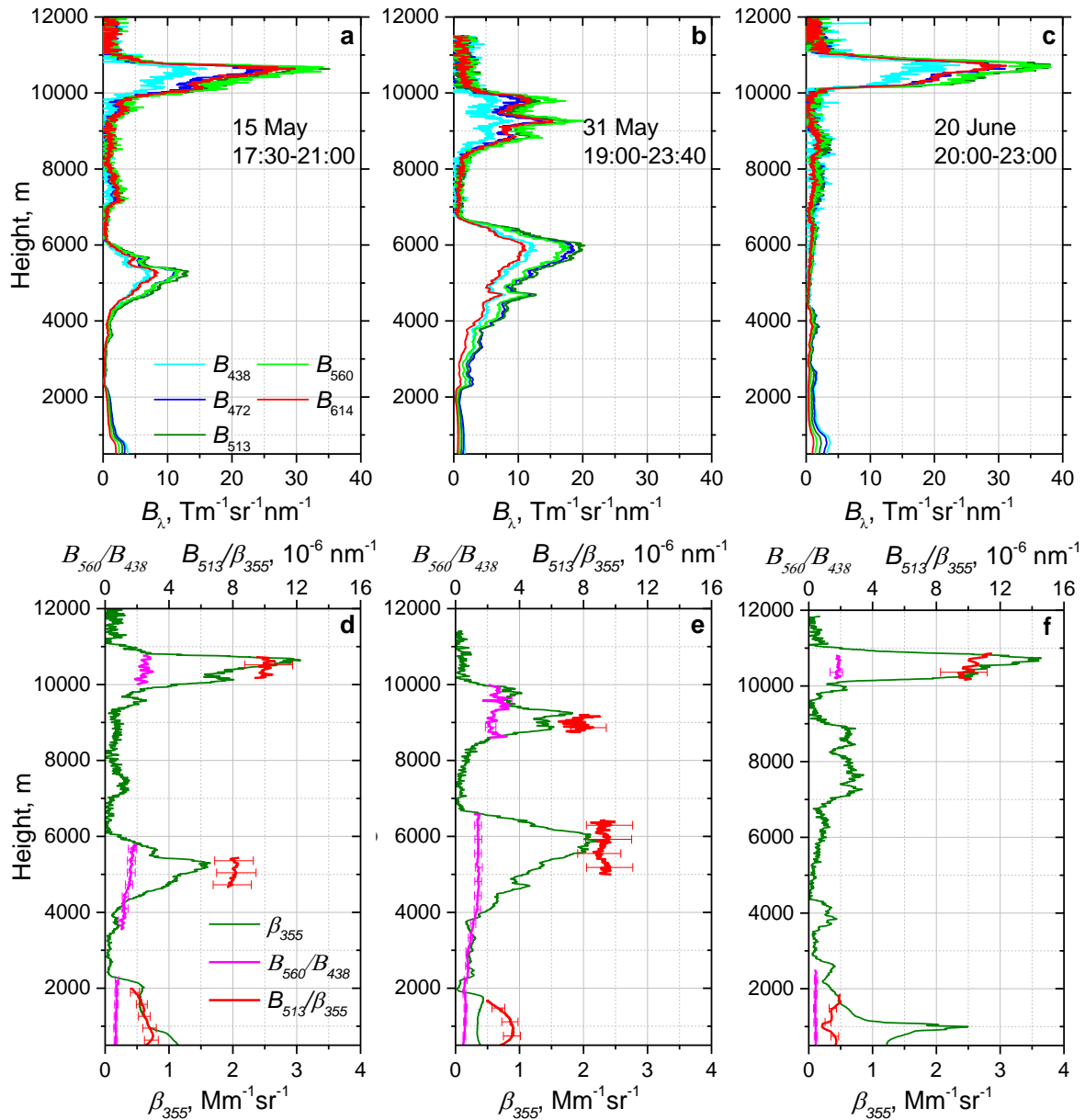
Fig.6. Particle hygroscopic growth in the PBL on the night 12-13 June 2023 over Lille. Spatio-temporal distributions of (a) aerosol backscattering coefficient  $\beta_{532}$  and (b) fluorescence backscattering  $\beta_F$  (in  $10^{-4} \text{ Mm}^{-1} \text{ sr}^{-1}$ ). Vertical profiles of (c) aerosol  $\beta_{532}$  and fluorescence  $\beta_F$  backscattering coefficients; (d) particle depolarization ratio  $\delta_{532}$  and the relative humidity RH; (e) fluorescence depolarization ratio  $\delta_F$  and fluorescence capacity  $G_F$  for the time period 21:00-22:15 UTC.

636  
637  
638



639  
640  
641  
642  
643

Fig.7. (a) Fluorescence depolarization ratio and (b) particle depolarization ratio  $\delta_{532}$  as a function of the relative humidity in the PBL for the measurements on 9, 10, 12, 13, 16 June 2023 over Lille.



644

645

646

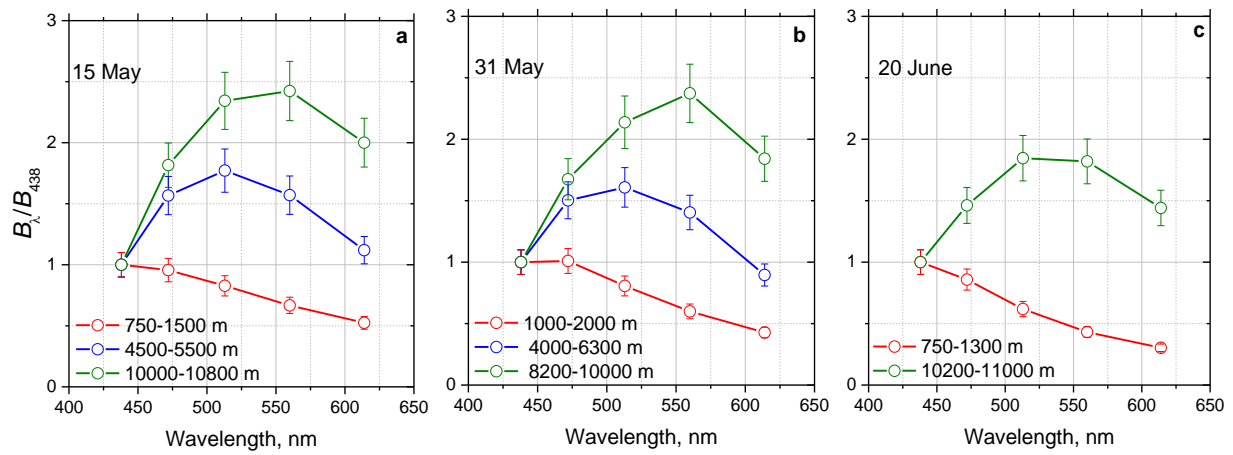
647

648

649

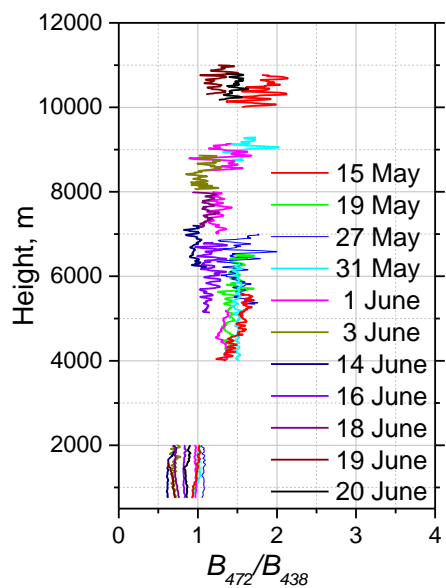
650

Fig. 8. Fluorescence measurements over Moscow on 15 May, 31 May, 20 June 2023. Vertical profiles of (a-c) fluorescence spectral backscattering coefficients  $B_\lambda$  at 438, 472, 513, 560, 614 nm and (d-f) aerosol backscattering coefficient  $\beta_{355}$ , the ratio  $B_{560}/B_{438}$  and  $B_{513}/\beta_{355}$ . Measurements were performed at an angle of  $48^\circ$  to horizon.



651

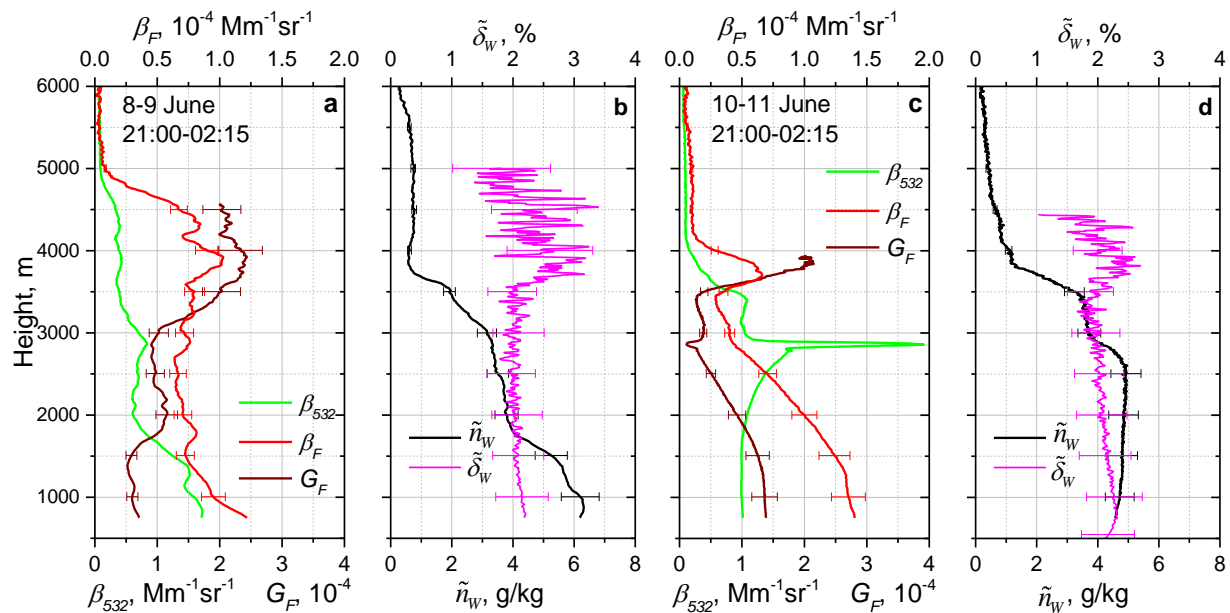
652 Fig.9. Fluorescence spectra  $B_\lambda/B_{438}$  at different height intervals measured during smoke episodes  
 653 on 15 May, 31 May, 20 June 2023 over Moscow, for the same temporal intervals as in Fig.8.  
 654



655

656 Fig.10. Height profiles of the ratio  $B_{472}/B_{438}$  for smoke episodes during 15 May – 20 June 2023  
 657 over Moscow. Smoke layers start above 4 km up to 11 km.

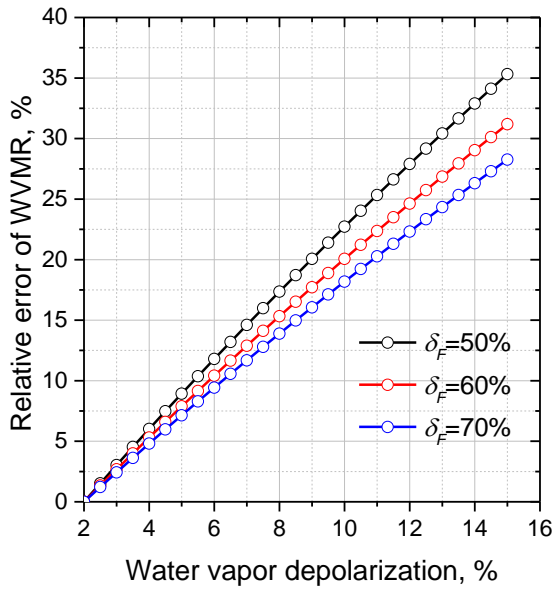
658



659  
 660  
 661  
 662  
 663  
 664  
 665

Fig.11. Impact of the aerosol fluorescence on the depolarization ratio in the water vapor Raman channel on the nights 8-9 and 10-11 June 2023 over Lille. Vertical profiles of (a, c) particle backscattering  $\beta_{532}$ , fluorescence backscattering  $\beta_F$ , fluorescence capacity  $G_F$  and (b, d) depolarization ratio  $\tilde{\delta}_W$  of the water vapor Raman signal and the water vapor mixing ratio  $\tilde{n}_W$ .





666

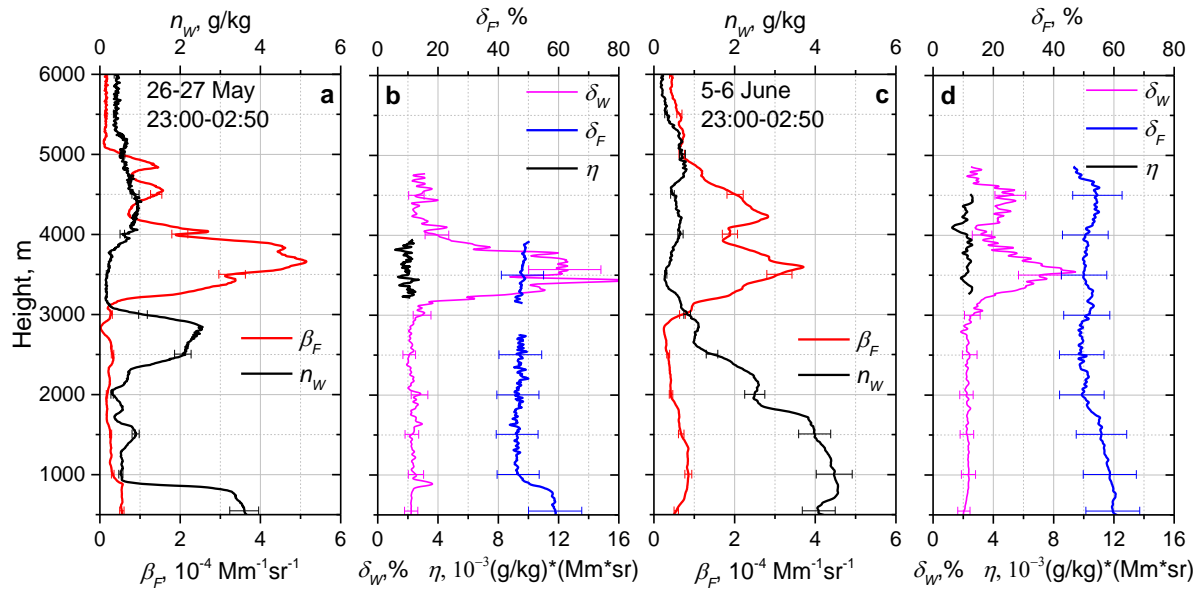
667 Fig.12. Relative error of water vapor mixing ratio (WVMR)  $\frac{\Delta n_w}{\tilde{n}_w}$  induced by the fluorescence as

668 a function of depolarization ratio  $\tilde{\delta}_w$  in the water vapor Raman channel for three values of  
 669 fluorescence depolarization ratio  $\delta_F=50\%$ ,  $60\%$ ,  $70\%$ . The depolarization ratio of water vapor  
 670 Raman backscatter in the absence of fluorescence is assumed to be  $\delta_w=2\%$ .

671

672

673  
674

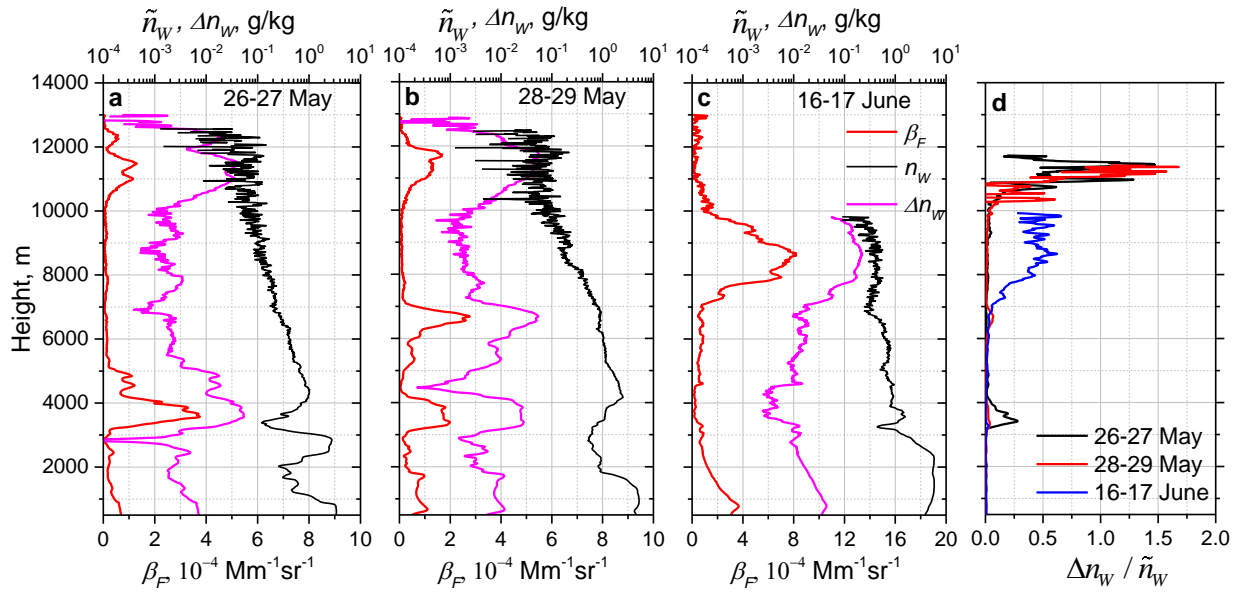


675

676 Fig. 13. Fluorescence measurements over Lille on the night 26-27 May and 5-6 June (a, c)  
677 Vertical profiles of the fluorescence backscattering  $\beta_F$ , the water vapor mixing ratio  $\tilde{n}_W$ , (b, d) the  
678 depolarization ratio of the water vapor Raman signal  $\tilde{\delta}_W$ , the fluorescence depolarization ratio  $\delta_F$   
679 and parameter  $\eta$ , describing contribution of the fluorescence to the water vapor channel.  
680

681

682



683

684

685

686

687

688

689

Fig.14. Impact of smoke fluorescence on the water vapor measurements. Vertical profiles of the fluorescence backscattering  $\beta_F$ , water vapor mixing ratio  $\tilde{n}_W$  and bias in water vapor channel  $\Delta n_W$  provided by the fluorescence of smoke for episodes on the nights (a) 26-27 May, (b) 28-29 May and (c) 16-17 June 2023 for time interval 21:00-02:30 UTC over Lille. (d) Error  $\frac{\Delta n_W}{\tilde{n}_W}$  introduced by smoke fluorescence for the three episodes.